Transparent alumina ceramics fabricated by 3D printing and vacuum sintering

David Carloni, Guangran Zhang, and Yiquan Wu*

Kazuo Inamori School of Engineering, New York State College of Ceramics, Alfred University,

Alfred, NY 14802, USA

*E-mail: wuy@alfred.edu

Abstract

Transparent alumina ceramics were fabricated using an extrusion-based 3D printer and post-processing steps including debinding, vacuum sintering, and polishing. Printable slurry recipes and 3D printing parameters were optimized to fabricate quality green bodies of varying shapes and sizes. Two-step vacuum sintering profiles were found to increase density while reducing grain size and thus improving the transparency of the sintered alumina ceramics over single-step sintering profiles. The 3D printed and two-step vacuum sintered alumina ceramics achieved greater than 99% relative density and total transmittance values of about 70% at 800 nm and above, which was comparable to that of conventional CIP processed alumina ceramics. This demonstrates the capability of 3D printing to compete with conventional transparent ceramic forming methods along with the additional benefit of freedom of design and production of complex shapes.

Keywords: transparent ceramics, 3D printing, additive manufacturing, alumina, vacuum sintering

1. Introduction

Since the invention of stereolithography by Charles Hull in the 1980's, 3D printing technology has grown and had a significant impact around the world in manufacturing complex

structures with excellent properties. 3D printing, also known as additive manufacturing, is a forming method where a 3D computer model is sliced into 2D cross-sections to construct a physical structure via the layer-by-layer addition of material. Within this general definition, there are many specific technologies which vary in terms of feedstock and method of forming/bonding to suite specific materials and applications. This is significantly different than more conventional subtractive or equivalent manufacturing methods that have been used for hundreds to thousands of years and allows for the fabrication of structures that would normally be impossible to create in a relatively fast and efficient manner. This has enabled different industries to create exciting new parts and products while also saving time and money and improving performance.[1-6]

Thus far, however, the main materials that have been utilized for 3D printing are polymers and metals, with ceramics being relatively less researched and developed. In recent years, though, there has been a significant increase in interest and use of ceramic materials along with 3D printing technologies due to the many useful applications of each. Ceramics, which are characterized by their excellent thermal, chemical, and electrical durability and stability, high strength and hardness, and useful optical properties, are ideal materials for applications in industries such as aerospace, medical, military and defense, electronics, and more.[3, 4, 7, 8] Although 3D printing has not yet fully matured, it is projected that in the future the market for 3D printing will increase in these industries as the technology continues to improve and become more assimilated into society.[3, 9-11]

Specifically, an area of application for 3D printing that is of interest to this work is in the fabrication of transparent polycrystalline ceramics.[12] Transparent polycrystalline ceramics have been well-demonstrated for use in many areas, such as for windows and domes,[13, 14] laser materials,[15, 16] armor[13, 17] and other applications which require high performance

even under potentially extreme environments.[18] Furthermore, along with their wide range of relatively inexpensive and efficient processing options, transparent polycrystalline ceramics have shown the ability to achieve thermal, mechanical, and optical properties which are comparable to, or even surpass, that of single crystals and glasses.[13, 14, 16, 17] To achieve these properties, it is necessary that the ceramic body simultaneously possess near full density, limited porosity, high purity, limited grain growth, and low surface roughness to reduce the amount of light scattering sources.[18, 19] Transparent polycrystalline ceramics have been primarily manufactured using methods such as dry pressing and cold isostatic pressing (CIP), tape casting, and mold casting followed by vacuum sintering, as well as others, such as hot isostatic pressing (HIP) and spark plasma sintering (SPS).[20, 21] All of these methods are capable of producing high-quality transparent polycrystalline ceramics, but are either unable to fabricate complex shapes or require additional tooling costs and processes to do so. With advances in 3D printing technology, however, it is currently possible to create near full density polycrystalline ceramic bodies which can be designed into custom shapes relatively quickly and easily. This potentially enables 3D printing to be used as a forming method for transparent ceramics, which could lead to interesting new opportunities and developments.

The chosen material for this work, alumina (Al_2O_3), is a well-known and widely used ceramic which has been demonstrated to achieve transparency and other useful properties[22-27] as well as be compatible with 3D printing[28-30]. Krell et al. reports the use of sintering and post-HIP treatment to produce near full density and submicron grained transparent alumina ceramics with 55-65% transmission in the visible wavelength range along with high hardness and bending strengths.[31] In a different study, Grasso et al. utilized high-pressure SPS to produce transparent alumina ceramics with 200 nm grain sizes that achieved 65.4% in-line

transmission at approximately 700 nm.[32] Of the many 3D printing methods and products available, an extrusion-based machine known as the Hyrel System 30M was chosen. In literature, this method can be referred to by different names, such as robocasting, direct ink writing (DIW), and more, but is characterized by its simplistic nature and ability to fabricate a wide variety of parts in a relatively fast and inexpensive manner.[1, 33-35] Furthermore, since the extrusion-based method does not require the use of photoactive polymers or other complex additives, more traditional ceramic processing principles can be applied. The goal of this work was to demonstrate and optimize the process of fabricating transparent polycrystalline ceramics via 3D printing and to compare the results to that of more conventional fabrication methods for transparent ceramics, such as cold isostatic pressing (CIP).

2. Material and Methods

2.1. Powder Preparation

The ceramic powder used was the Baikalox High Purity CR 10D Al_2O_3 powder with 625 ppm MgO (Baikowski, Inc.); in this powder, the MgO acts as a sintering aid. The as-received powder was ball-milled in ethanol for 24 hours using high-purity zirconia milling media of approximately 2mm in diameter and then dried and obtained using a mortar and pestle. The prepared powder was measured for particle size and distribution using a Micromeretics SediGraph III PLUS, specific surface area (SSA) using the BET method and a Micromeretics FlowPrep to de-gas the sample followed by measurement with a Micromeretics Gemini VII, and for morphology using an FEI Quanta 200F SEM.

2.2. Slurry Preparation

Fabrication of ceramic parts with the Hyrel 3D System 30M extrusion-based 3D printer requires preparation of a high solids-loading ceramic slurry. The ceramic slurry consisted of the

following batch recipe: 68-74 weight percent (wt.%) Baikalox High Purity CR 10D Al_2O_3 powder with 625 ppm MgO, 26-32 wt% DI H_2O, and 0.4-1.0 wt% Kuraray ISOBAM™-104 per mixed Al_2O_3 powder. In this batch, the isobam acts as a binder and dispersant. The slurry was prepared by combining the batch ingredients in a shear mixer until a viscous paste is formed. High purity zirconia milling media of approximately 1 cm in diameter was added to the milling jar and the jar was placed in a ball mill to mix for 1 - 1.5 hours. Once homogenized, the slurry was loaded into a shear mixer within a customized vacuum chamber to de-gas for at least 15 minutes, or until all bubbles are removed. The resulting slurry was directly loaded into an EMO-25 extruder which was fitted with a chosen nozzle and used for 3D printing or used for rheology measurements as will be specified later.

2.3. 3D Printing

Various parts for 3D printing in the .stl file format were directly uploaded to the Hyrel 3D System 30M 3D printer's Repetrel software. The part file was edited in terms of dimensions and orientation as desired and then sliced into "G-code" (programming language for 3D printing) using the built-in Slic3r software according to pre-determined printing parameters. The printing parameters were adjusted in Slic3r according to the size of the part, nozzle size, and other factors. After slicing into G-code is complete, a mylar film was taped onto the build platform for the part to be built upon. The gap between the extruder and build platform was set by placing a piece of paper (standard 8.5" x 11" copy paper; 75-80 g/m^2) on the build platform and using the "z-calibrate" feature to move the platform until the tip of the nozzle on the extruder barely contacted the paper. Once the gap was set, the extruder was primed until material flowed out of the nozzle at a consistent rate, afterwards the print job was started. The print job was then observed, with small changes made using the "z fine-adjustment" feature, which moves the

platform vertically by 25 µm, to ensure that the distance between the extruder and build platform/part was sufficient. Following printing, the mylar sheet with the finished part on it was removed from the build platform and left to dry underneath a cover inside of an auto-desiccator. More print jobs were performed as necessary using the same process. Green body density was measured where possible on the 3D printed parts using a dial caliper and balance (limited to simple shapes).

2.4. CIP Processing

As a conventional processing method to compare 3D printing with, CIP was employed. CIP samples were fabricated using the as-prepared Baikalox CR 10 D High Purity Al_2O_3 powder with 625 ppm MgO (same powder used in 3D printing) combined with approximately 0.25 mL of PVA via a mortar and pestle until homogenized. The resulting powder was dry-pressed into a disk of approximately 2 cm in diameter using a Carver Inc. manual uniaxial press with a pressure of 1 metric-ton for 5 seconds and then cold isostatically pressed at 250 MPa for 1 minute using an Autoclave Engineers CP 360 to form a dense green body. The green body density of the CIP parts was measured using a dial caliper and balance.

2.5. Drying, Debinding, and Sintering

The finished 3D printed parts were dried for 24 hours in air at room temperature in an auto-desiccator. Next, the parts were placed in a Quincy Lab, Inc. Model 30 GC Lab Oven held at 70°C to dry for an additional 24 hours. The oven dried 3D printed parts as well as the CIP parts were then debinded in a Neytech Vulcan Benchtop Furnace Model 3-550 under the following profile: heat from room temperature to 500°C at a rate of 0.5°C/min, hold at 500°C for 4 hours, heat from 500°C to 1000°C at a rate of 1°C/min, hold at 1000°C for 3 hours, auto-cool to room temperature. The debinded samples were placed into a Thermal Technolgy Inc. High Vacuum

Graphite Furnace to sinter under the following profile with varying final temperatures from 1650 – 1875°C: heat from room temperature to 1300°C at a rate of 10°C/min, hold at 1300°C for 1 hour, heat from 1300°C to the final sintering temperature, hold at final temperature for 6 hours, and cool to room temperature at 10°C/min; this is a conventional single-step sintering (SSS) profile. As an alternative to the SSS profile, a two-step sintering (TSS) profile was also investigated with the sample being heated to a final temperature of 1850°C or 1875°C and then immediately dropping to 1800°C prior to holding for 8 hours.

2.6. Testing and Characterization

The sintered parts were tested and characterized for different properties. Density was determined using the Archimedes method. Following density measurements, the samples which achieved good visual transparency were grinded and polished to an approximately 1.5 mm thickness using a Buehler EcoMet 3000 Variable Speed Grinder-Polisher and a MetLab Corporation 6 µm diamond suspension. Total transmittance measurements were conducted on the polished sample using a Thermo Scientific Evolution 220 UV-Visible Spectrophotometer in the wavelength range from 190 -1100 nm. The microstructure was documented by gold-coating the sample using a Cressington Sputter Coater 108 and viewing and capturing images of the sample on an FEI Quanta 200F Scanning electron microscope. Grain size measurements were conducted using the line intercept method and the Nano Measurer 1.2 software. A minimum of 100 grains were measured from multiple locations per sample (approximate span of 300,000 µm^2) to determine an average grain size and standard deviation directly from the SEM images without applying a correction factor.

When measuring the rheology of the slurry instead of 3D printing, the slurry was prepared under the same parameters according to the batch recipes used for printing. The slurry was then

measured using a TA Instruments Discovery HR-2 Hybrid Rheometer to obtain curves of viscosity as a function of shear rate at room temperature under the flow sweep procedure at shear rates from $0.01 - 100$ s^{-1} using the 40 mm parallel plate geometry. Flow behavior was calculated directly from the curve of viscosity as a function of shear rate using the power law function in **Equation 1**:

$$\eta = K\dot{y}^{(n-1)} \tag{1}$$

where η is the viscosity, $\dot{y}$ is the shear rate, K is the consistency index (viscosity at $\dot{y}=1$), and n is the power law index (also known as flow index). Different flow index values indicate different behaviors: n = 1 is Newtonian, n > 1 is shear thickening, and n < 1 is shear thinning.[36, 37]

3. Results and Discussions

Al$_2$O$_3$ ceramic parts of varying shapes and sizes were successfully fabricated using 3D printing. Near full-density and transparency was achieved in the 3D printed samples via post-processing steps, including debinding, vacuum sintering, and polishing. **Fig. 1** shows photographs of various 3D printed parts and **Fig. 2** shows the results of each processing step on the ceramic body.

Fig. 1. Photographs of 3D printed alumina ceramics of varying shapes and sizes
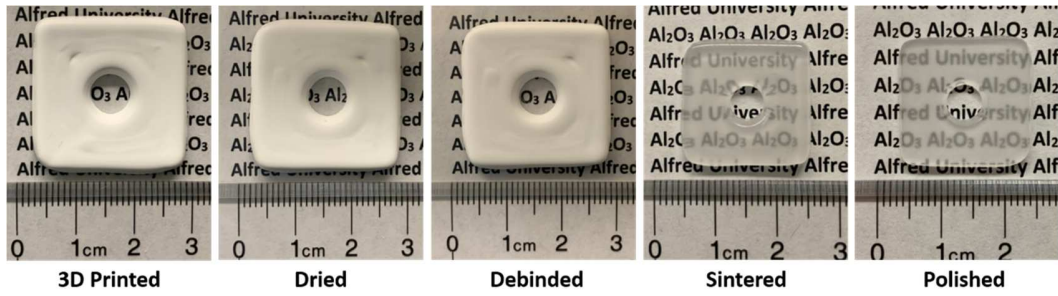
Fig. 2. Photographs of representative 3D printed sample through each step of the process.

3.1. Alumina Powder

The particle size and distribution data, as shown in **Fig. 3**, indicates that the particles were of submicron size with a relatively narrow distribution. The particle size with the highest mass-frequency was 0.596 µm and the D10, D50, and D90 were 0.384, 0.731, and 2.238 µm, respectively. The SSA as measured using the BET method was 7.9571 ± 0.1174 m^2/g. An SEM image of the powder is presented in **Fig. 4**, which shows that the particles are nearly spherical in shape and mostly uniform. The small size, high surface area, and nearly spherical shape of the powder indicate good potential packing efficiency and densification behavior during sintering.
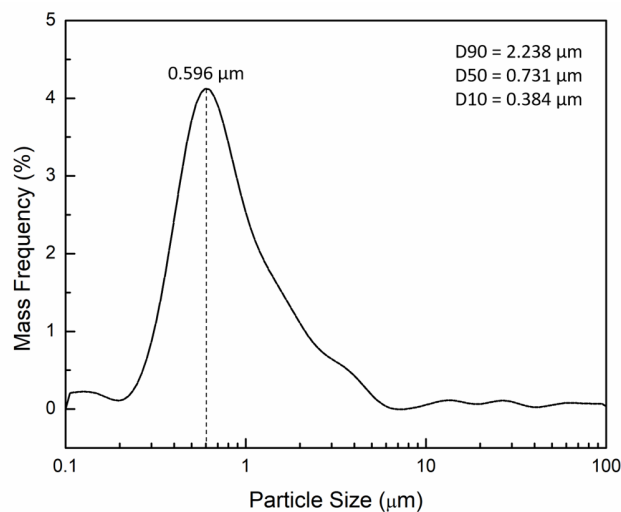
Fig. 3. Particle size and distribution of the as-prepared Baikalox CR 10D Al$_2$O$_3$ powder with 625 ppm MgO.
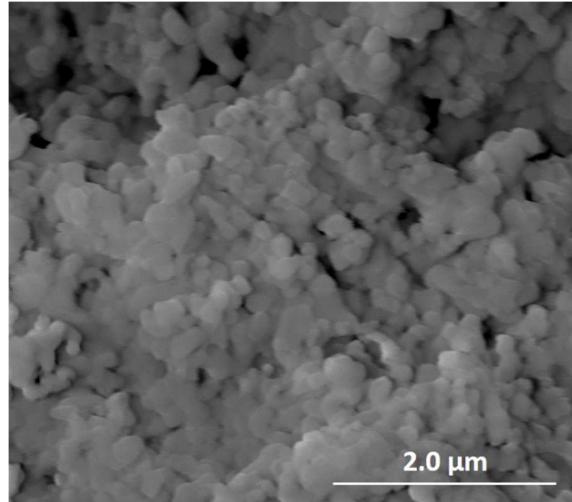
Fig. 4. SEM image of the as-prepared Baikalox CR 10D Al_2O_3 powder with 625 ppm MgO.

3.2. Slurry Batch Recipes and Rheology

The slurries contained varying amounts of alumina content as well as isobam per mixed powder as a binder and dispersant. Both batch ingredients significantly affected the rheology of the slurry and thus the printing behavior. **Fig. 5** and **Fig. 6** present the results of the rheology measurements for slurries with varying amounts of alumina and isobam per mixed powder, respectively, along with the calculated flow index (n) values according to the aforementioned Equation 1 from section 2.5. The viscosity measurements in Fig. 5 and 6 indicate that increases in the content of alumina and isobam per mixed powder by increments of 2 wt% and 0.3 wt%, respectively, can result in as much as an order of magnitude increase in viscosity. Furthermore, it can be seen that every slurry measured exhibited a flow index value less than 1, indicating shear-thinning behavior.

In practice, higher viscosity slurries tended to exhibit greater control and shape retention during printing than the lower viscosity slurries. On the other hand, the higher viscosity slurries tended to be more difficult to prepare in terms of achieving a homogeneous mixture and thoroughly de-gassing. Therefore, it was necessary to maintain a balance between these

parameters. In this case, slurries with 68 – 74 wt% alumina and 0.4 – 1.0 wt% isobam per mixed powder are considered "printable", with the slurry containing 72 wt% alumina and 0.7 wt% isobam per mixed powder being ideal for printing. Below this range, slurries are not sufficiently viscous for printing and above this range, slurries are too viscous to be properly prepared for printing.

Furthermore, the shear-thinning (pseudoplastic) behavior is essential for 3D printing and was exhibited in every slurry tested. Shear-thinning describes a decrease in viscosity with increasing shear rate.[36] Practically speaking, this indicates a transitional period of rheological behavior before, during, and after extrusion with the 3D printer. This therefore enables a high viscosity slurry to become fluid enough to be extruded through a small nozzle and then return to a higher viscosity state, allowing for proper flow and workability during printing without sacrificing final shape retention and control.
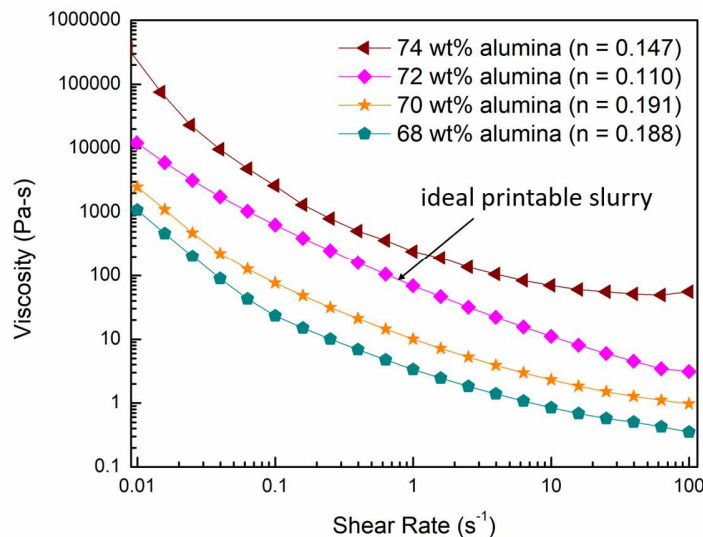
Fig. 5. Viscosity as a function of shear rate for slurries with varying alumina content and constant 0.7 wt% isobam per mixed powder with corresponding flow index (n) values in parentheses.
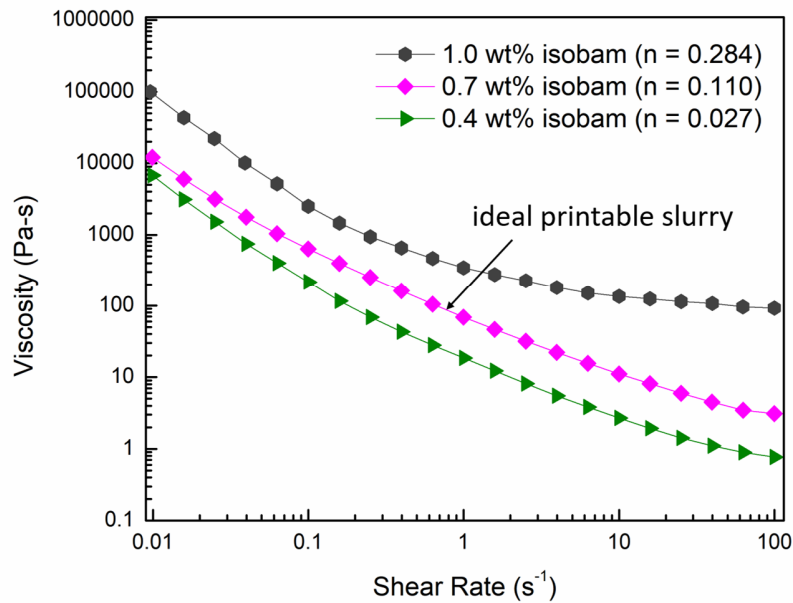
Fig. 6. Viscosity as a function of shear rate for slurries with varying isobam content per mixed powder and constant 72 wt% alumina with the corresponding flow index (n) values in parentheses.

3.3. 3D Printing Parameters

For printing parameters, there were a variety of options available, of which only a few were found to be both relevant and significant to this work: printing speed, nozzle size, extrusion width, and layer height. In general, decreasing the printing speed, nozzle size, extrusion width, and layer height typically results in higher quality parts, but leads to slower extrusion rates and longer printing times. Excessively long printing times and extrusion rates were observed to cause problems such as premature drying leading to poor interlayer adhesion and clogging of the nozzle. Overall, the average green body density across the 3D printed samples was 1.68 ± 0.05 g/cm^3, but there were some differences among parts printed with different parameters. In comparison, the CIP parts achieved a slightly higher and more consistent green density of $1.71 \pm$

0.04 g/cm^3, likely due to the less variability in the process and additional compaction of the green body through CIP. Similar to the slurry parameters, it is necessary to find a well-balanced set of printing parameters which produce quality parts in the proper time frame.

3.3.1. Printing and Non-Printing Speed

The movements that the printer performs can be generally classified into two groups: printing moves and non-printing moves. Printing moves are the movements where material is being actively extruded to build the part. It was found that if this parameter was set too fast, there would be poor interlayer adhesion and inconsistent formation of layers/surfaces resulting in a low quality and dimensionally inaccurate structure. However, if the speed was set too slow, the print would take excessively long and the low throughput of material would result in premature drying and clogging of the nozzle. It was determined that print move speed in the range of 1.5 – 4.0 mm/s was ideal for this work, with the slower end of the range being used for smaller and more complex parts and the faster end used for larger and more simple parts.

Non-printing moves are any movement that doesn't directly contribute to building the part, such as moving up a layer and moving across gaps. During these movements, no material is intentionally being deposited although it was found that excess material will occasionally continue to "ooze" out of the nozzle following a recent print move. For these reasons, this parameter is relatively insignificant as long as it is set fast enough to prevent material from inadvertently oozing onto the part being built. A value of 40 mm/s was used for this parameter and that was found to be sufficient.

3.3.2. Nozzle Size, Layer Height, and Extrusion Width

Nozzle size, layer height, and extrusion width are all interconnected. These parameters effect the extrusion rate, how long the print takes, and the overall accuracy. In all cases, larger values result in more material being extruded at a faster rate along with shorter printing times and overall lower accuracy, while smaller values have the opposite effect. As the names indicate, the layer height controls how tall each layer is and therefore how many layers comprise the part, the extrusion width controls how wide of a path of material the extruder deposits and therefore how many paths are required to fill in a structure, and the nozzle size is the inside diameter of the chosen nozzle.

Depending upon the size of the part, certain nozzle sizes are more appropriate. If a relatively large nozzle size (1.20 mm or larger) is chosen for a small part with fine details, the nozzle will be inherently incapable of producing it well. On the other hand, if a small nozzle (0.41 mm or smaller) is chosen for a large part, the part will take excessively long to print. As a general guideline and recommendation based on observations, the nozzle size should not exceed about 20% of the smallest feature size nor be smaller than about 4% of the longest dimension of the structure to maximize quality and efficiency.

For layer height, it was determined that a value between approximately 25 - 70% of the nozzle diameter was suitable for printing. When the layer height was larger than 70%, despite having a fast print time, there was an excess of material being extruded which led to slumping and low dimensional accuracy. However, when the layer height was less than 25%, the layers were too thin and the print time was too long, resulting in pre-mature drying and poor interlayer adhesion/formation. In between this range, adequate parts could be built. **Fig. 7** shows the calculated printing time as a function of layer height for a part being printed with a 0.84 mm

nozzle. It can be seen that as the layer height increases, the printing time decreases, until around 0.4 mm (~48% of nozzle), after which there is not a significant decrease in printing time. This indicates that there is no significant additional benefit in increasing the layer height past this point, making a value of ~48% an ideal balance between quality and efficiency. It was also found that the layer height does more than effect the part visually. When five identical parts were all printed with a 0.84 mm nozzle, but with different layer heights, there was a significant difference in their green densities. **Fig. 8** shows the green body density as a function of layer height along with inset photographs of actual samples, and it can be seen that the density decreases significantly with increasing layer height. This is likely due to two observable tendencies. First, parts with small layer heights tend to have smaller defects that are "corrected for" or "covered up" by the many layers which are printed on top of it as opposed to parts with large layer heights which typically have larger defects and less subsequent layers to fix the problem. Second, parts with large layer heights tend to form more loosely packed edges with necking in between layers as opposed to the small layer height parts which form more densely packed layers and edges as supported by the inset photographs in Fig. 8. Additionally, when these five parts were sintered under constant parameters (1850°C for 6 hours), there was again a significant difference in their sintered relative densities. **Fig. 9** shows the relative sintered density of the five parts as a function of their layer height. It can be seen again that as the layer height increases, the relative density decreases. These results show that the final sintered density is dependent upon the green density achieved, thus further supporting the importance of selecting proper printing parameters, such as layer height.
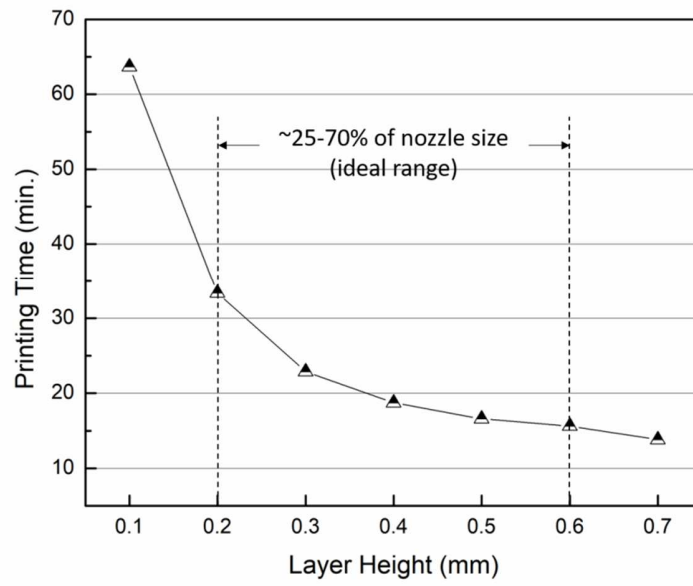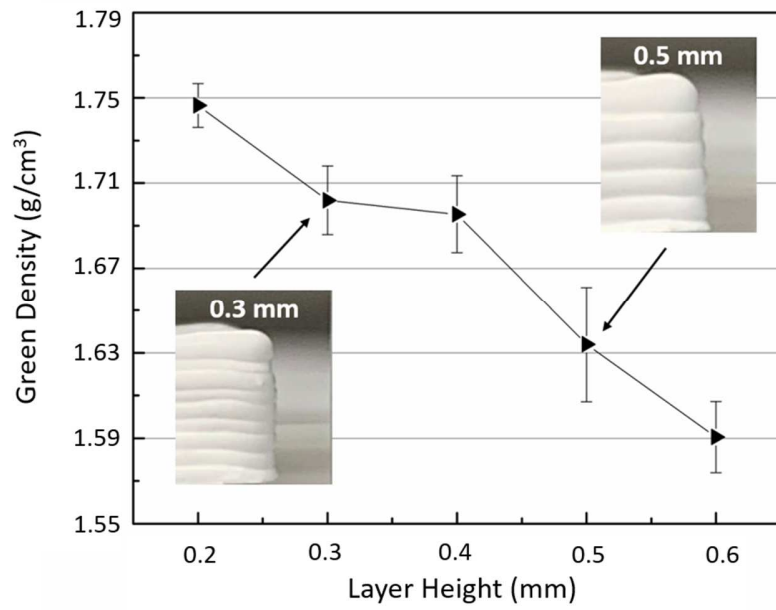
Fig. 7. Printing time as a function of layer height.

Fig. 8. Green body density as a function of layer height with inset photographs of actual samples.
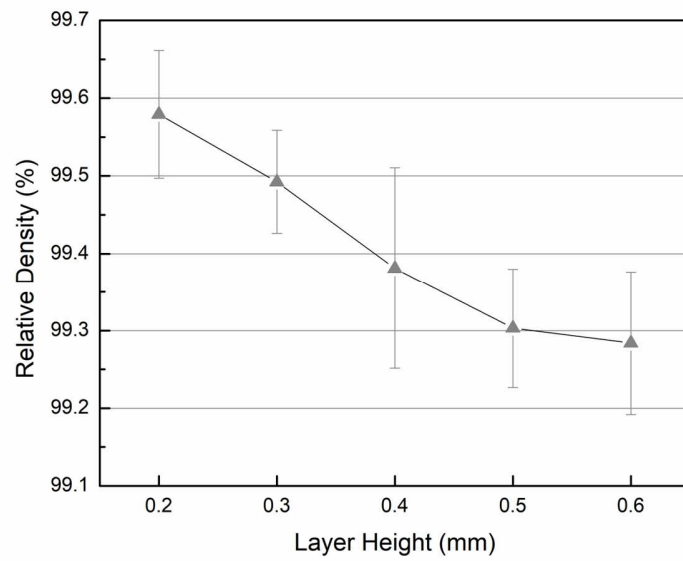

Fig. 9. Relative density as a function of layer height for samples sintered at 1850°C for 6 hours.

For extrusion width, this parameter needs to be just large enough to sufficiently infill the part and create a dense green body. A value of approximately 150% of the nozzle size is sufficient for this by creating an overlap between each printing path, thus ensuring complete infill without noticeable changes in surface/edge finish or dimensional accuracy. **Fig. 10** shows the results of using vastly different extrusion width values to clearly demonstrate its effect. When the extrusion width is too small, there are gaps in the structure, and when the extrusion width is too large, there is a loss in accuracy and fine finishes on the surface/edge. When the parameters are set properly, however, it can be seen that a filled-in structure with a fine finish along the surface and edges as well as good dimensional accuracy is achieved.
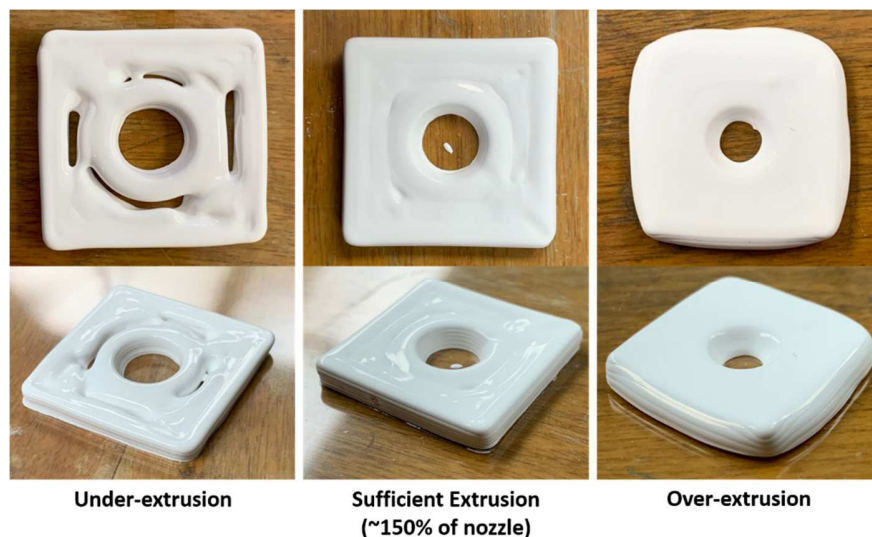

Fig. 10. Photographs of samples which were 3D printed at varying extrusion widths.

3.4. Post-Processing and Testing

The drying and debinding parameters were chosen to remove the water and binder content in a slow and controlled manner to prevent cracking in the green body. Drying for 24 hours in air within an auto-desiccator and an additional 24 hours in an oven held at 70°C followed by

debinding up to 500°C at 0.5°C/min for 4 hours and then up to 1000° at 1.0°C/min for 3 hours accomplished this task and these parameters were held constant during all experimentation.

Sintering parameters were varied in terms of both final temperature and holding time. Furthermore, single-step sintering (SSS) and two-step sintering (TSS) profiles were investigated. The relative density of the 3D printed and CIP samples as function of the sintering profile is plotted in **Fig. 11** and it can be seen that across all samples there was an increase in density with sintering temperature as well as that both the 3D printed and CIP processed ceramics reached similar peak density values at the highest tested temperature of 1875°C. The peak density values achieved by 3D printing were 99.91 ± 0.08% for SSS and 99.92 ± 0.03% for TSS while the highest CIP density achieved was 99.93 ± 0.05% under a TSS profile. Furthermore, the average grain size of the 3D printed samples under different sintering profiles is plotted in **Fig. 12** and representative SEM images of the microstructure of the SSS and TSS ceramics are presented in **Fig. 13 and Fig. 14**, respectively, which shows the dense microstructure that is free of pores and secondary phases as well as the mostly uniform grain size distribution**.** As mentioned previously, the grain size measurements were collected from multiple SEM images in different locations on at least 100 grains (approximate span of 300,000 μm^2) to determine an average and standard deviation. It can be seen that the average grain size increases with sintering temperature and that there is a decrease in grain size from SSS to TSS. For example, at 1875°C, the SSS sample had an average grain size of 113.27 ± 17.48 µm while the TSS sample had an average grain size of 87.69 ± 13.53 µm. These results, combined with the relative density measurements, indicate that TSS profiles can help to densify the 3D printed ceramics while limiting grain growth.
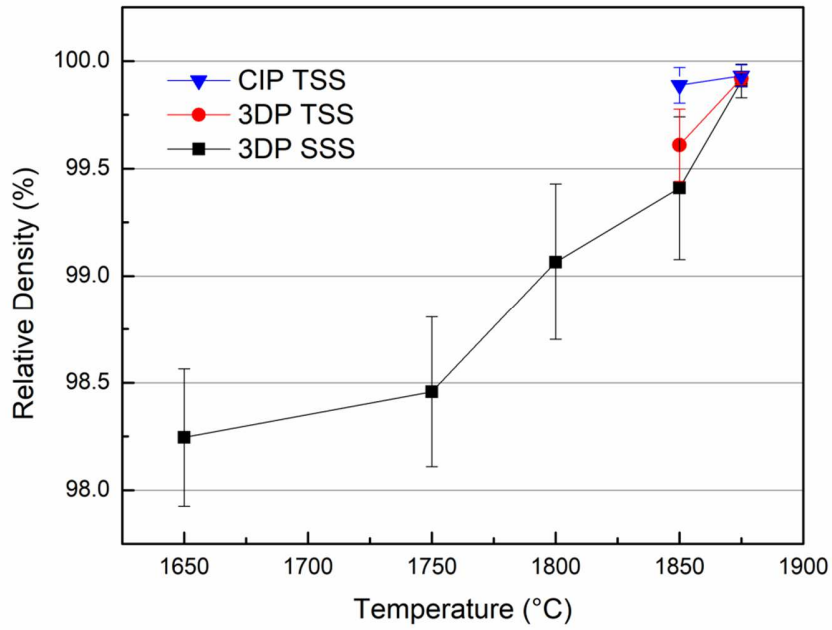
Fig. 11. Relative density as a function of sintering temperature for 3D printed and CIP processed alumina ceramics sintered under single-step (SSS) and two-step (TSS) sintering profiles.
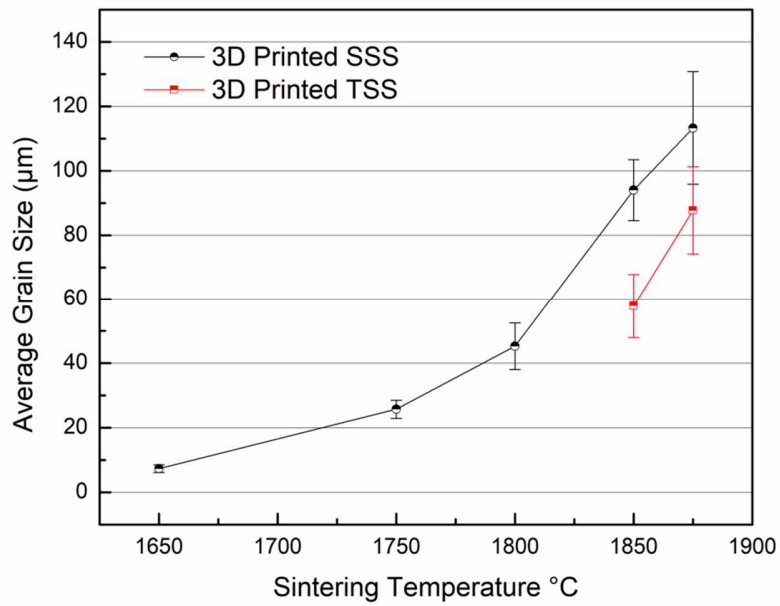

Fig. 12. Average grain size as a function of sintering temperature for 3D printed alumina ceramics sintered under single-step (SSS) and two-step (TSS) sintering profiles.
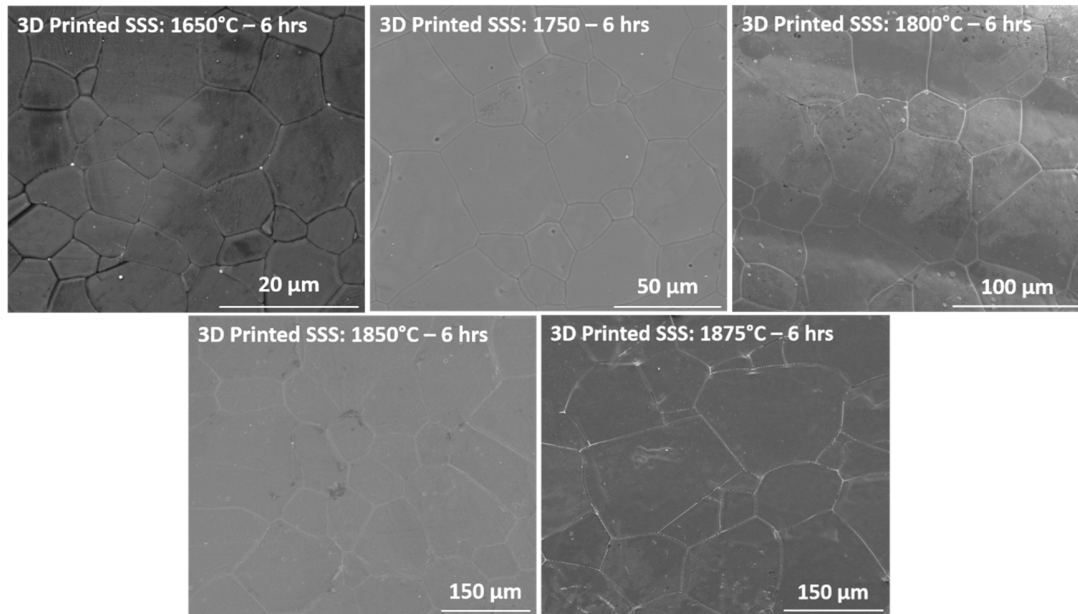
Fig. 13. Representative SEM microstructure images of 3D printed samples which were single-step sintered (SSS) at varying temperatures for 6 hours.
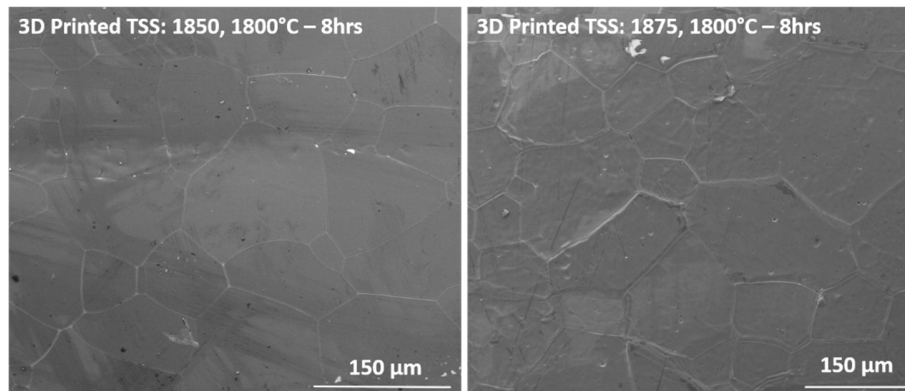

Fig. 14. Representative SEM microstructure images of 3D printed samples which were two-step sintered (TSS) at varying peak temperatures.

The most visually transparent 3D printed (both SSS and TSS) and CIP processed samples were grinded and polished to an approximately 1.5 mm thickness and measured for total transmittance as plotted in **Fig. 15,** along with inset photographs of the actual samples. It can be seen from both the data and the photographs that the best 3D printed and CIP processed ceramics

achieved similar levels of transparency. The total transmittance measurements showed that the 3D printed and CIP processed TSS ceramics reached nearly identical maximum values of approximately 70 - 71% at wavelengths of 800 nm and above (near IR range). In the visible wavelength range (~400 -700 nm), however, there was a more significant measurable difference, with the CIP sample being the most transparent followed in order by the 3D printed TSS samples at 1875°C and 1850°C, respectively. This slight drop-off in transparency from CIP to 3D printing is likely due to any defects introduced in the printing process limiting the density which can be achieved through sintering. The 3D printed SSS samples were significantly less transparent than the rest and reached a peak of only about 63% transmission at 800 nm and above when sintered at 1850°C; this is because the SSS samples have both lower densities and larger grain sizes than the other samples. These results demonstrate that 3D printed ceramics can achieve similar optical properties to CIP processed ceramics and that TSS profiles can yield improved transparency over SSS profiles.
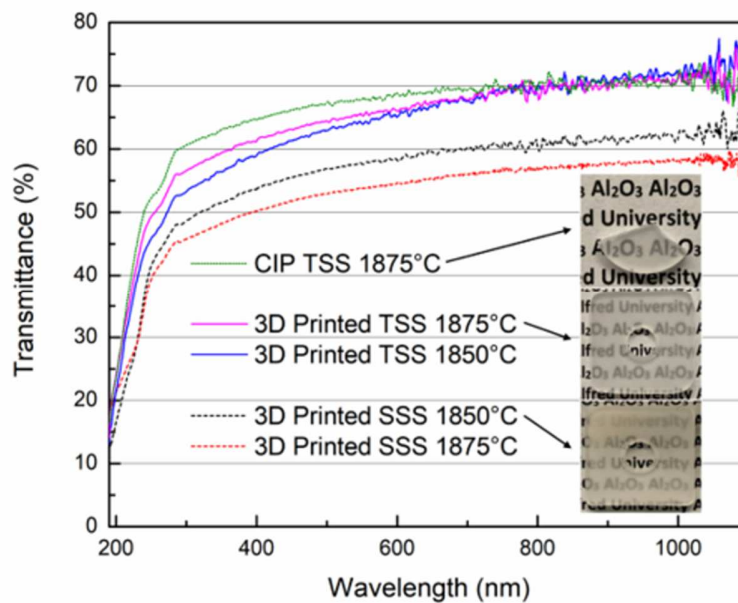
Fig. 15. Measured total transmittance spectra for 3D printed and CIP processed alumina ceramics sintered under single-step (SSS) and two-step (TSS) sintering profiles along with photographs of the actual samples.

In comparison to the results of other works in literature, the 3D printed samples in this report were able achieve similar results. Kim et al. reported on SPS processed alumina ceramics of 1 mm thickness which achieved a maximum total transmittance of approximately 70% at 800 nm and greater than 80% at 1000 nm and above.[38] Yang et al. also reported on 1 mm thick transparent alumina ceramics fabricated by isostatic pressing and sintering in H_2 atmosphere which achieved a total transmittance as high as 86% from 300-800 nm.[39] These values from literature are higher than what was achieved in this report, which is likely due to the significant difference in thickness between the samples (1 mm vs 1.5 mm), since transmittance decreases with increasing sample thickness. For this reason, the transmittance values for the most transparent 3D printed and CIP samples (both TSS up to 1875°C) were calculated at different sample thicknesses using the Beer-Lambert Law, shown in **Equations 2 and 3** below[40]:

$$A = \alpha d \tag{2}$$

$$A = 2 - \log(T) \tag{3}$$

where A is the absorbance, α is the absorption coefficient, d is the sample thickness, and T is the transmittance. The calculated transmittance values are plotted in **Fig. 16**. This data shows how the transmittance decreases with sample thickness. At a thickness of 1.0 mm, the 3D printed and CIP samples reach peak transmission values of approximately 78-80% at 800 nm and above, which is higher than that reported by Kim et al. (~70%) and slightly lower, but still comparable to, the report from Yang et al. at the same thicknesses (1.0 mm) and wavelengths (~800 nm).
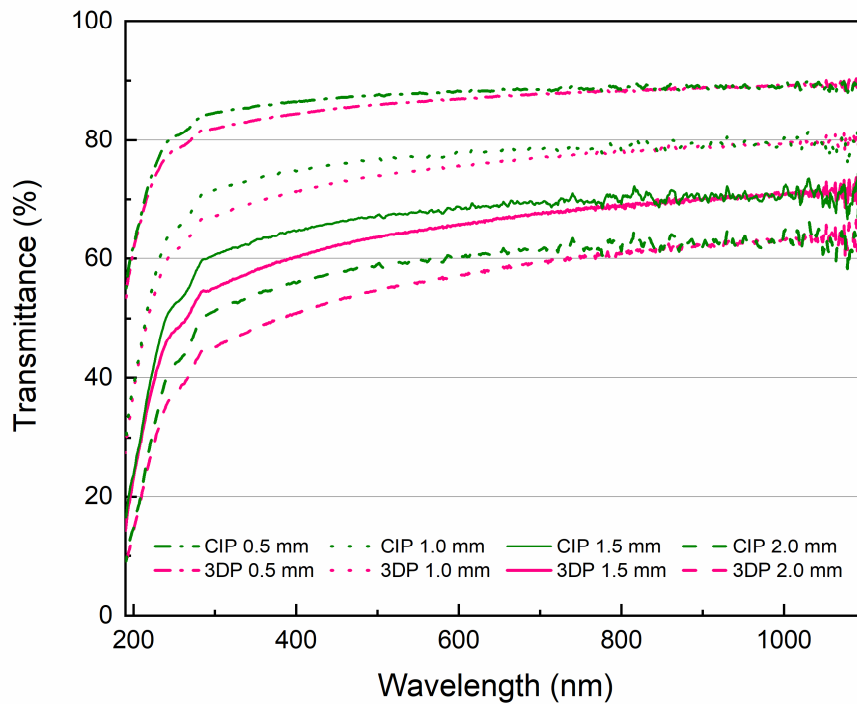
Fig. 16. Calculated total transmittance spectra as a function of sample thickness using the Beer-Lambert Law for the most transparent 3D printed and CIP samples (both two-step sintered up to 1875°C).

4. Conclusions

Using an extrusion-based 3D printer and post-processing steps, including debinding, vacuum sintering, and polishing, it has been demonstrated that near full-density (greater than 99% relative density) transparent ceramics of varying shapes and sizes can be fabricated which are of optical quality comparable to that achieved by more conventional processing methods for transparent ceramics, such as CIP. The highest quality 3D printed transparent ceramics were achieved through the use of optimized slurry and printing process parameters as well as a two-step sintering profile. With conventional methods, fabricating transparent ceramics of varying shapes and sizes would require additional tooling costs and processes. In this report, the same 3D

printer and process was used throughout, with only slight adjustments made to specific parameters. Furthermore, the simplistic nature of the extrusion-based 3D printer, as compared to other 3D printing methods, along with the aqueous slurry and use of a vacuum furnace, allows for conventional ceramic processing principles and know-how to be applied relatively easily, making the entire process more accessible to a larger population. In this way, customizable transparent ceramic structures can be made with greater relative ease and efficiency via 3D printing and vacuum sintering when compared with conventional methods without a significant difference in quality.

Declaration of Competing Interests

The authors of this manuscript, "Transparent alumina ceramics fabricated by 3D printing and vacuum sintering" have no conflicts of interest to declare.

Acknowledgements

References

[1] Z. Chen, Z. Li, J. Li, C. Liu, C. Lao, Y. Fu, C. Liu, Y. Li, P. Wang, Y. He, 3D printing of ceramics: A review, J. Eur. Ceram. Soc. 39(4) (2019) 661-687.
[2] B. Lu, D. Li, X. Tian, Development Trends in Additive Manufacturing and 3D Printing, Engineering 1(1) (2015) 85-89.
[3] T. Ngo, A. Kashani, G. Imbalzano, K. Nguyen, D. Hui, Additive manufacturing (3D printing): A review of materials, methods, applications and challenges, Composites, Part B 143 (2018).
[4] K.V. Wong, A. Hernandez, A Review of Additive Manufacturing, ISRN Mech. Eng. 2012(4) (2012) 1-10.
[5] M. Bechthold, Ceramic prototypes - design, computation, and digital fabrication, Inf. Constr. 68(544) (2016) 1-11.
[6] A. Zocca, P. Colombo, C.M. Gomes, J. Günster, Additive Manufacturing of Ceramics: Issues, Potentialities, and Opportunities, J. Am. Ceram. Soc. 98(7) (2015) 1983-2001.

[7] L.J. Kumar, C.G. Krishnadas Nair, Current Trends of Additive Manufacturing in the Aerospace Industry, in: D.I. Wimpenny, P.M. Pandey, L.J. Kumar (Eds.), Advances in 3D Printing & Additive Manufacturing Technologies, Springer Singapore, Singapore, 2017, pp. 39-54.

[8] A.A. Zadpoor, J. Malda, Additive Manufacturing of Biomaterials, Tissues, and Organs, Ann. Biomed. Eng. 45(1) (2017) 1-11.

[9] M. Sebastian, K. Omera, 3D Printing and Its Disruptive Impacts on Supply Chains of the Future, Technology Innovation Management Review 5(11) (2015).

[10] B. Berman, 3-D printing: The new industrial revolution, Business Horizons 55(2) (2012) 155-162.

[11] R. Jiang, R. Kleer, F.T. Piller, Predicting the future of additive manufacturing: A Delphi study on economic and societal implications of 3D printing for 2030, Technological Forecasting and Social Change 117 (2017) 84-97.

[12] R. Johnson, P. Biswas, P. Ramavath, R.S. Kumar, G. Padmanabham, Transparent Polycrystalline Ceramics: An Overview, Transactions of the Indian Ceramic Society 71(2) (2012) 73-85.

[13] J.A. Salem, Transparent Armor Ceramics as Spacecraft Windows, J. Am. Ceram. Soc. 96(1) (2013) 281-289.

[14] X.J. Liu, F. Chen, F. Zhang, H.L. Zhang, Z. Zhang, J. Wang, S.W. Wang, Z.R. Huang, Hard transparent AlON ceramic for visible/IR windows, Int. J. Refract. Met. Hard Mater. 39 (2013) 38-43.

[15] J. Sanghera, W. Kim, G. Villalobos, B. Shaw, C. Baker, J. Frantz, B. Sadowski, I. Aggarwal, Ceramic Laser Materials, Mater. 5(2) (2012) 258-277.

[16] J. Sanghera, S. Bayya, G. Villalobos, W. Kim, J. Frantz, B. Shaw, B. Sadowski, R. Miklos, C. Baker, M. Hunt, I. Aggarwal, F. Kung, D. Reicher, S. Peplinski, A. Ogloza, P. Langston, C. Lamar, P. Varmette, M. Dubinskiy, L. DeSandre, Transparent ceramics for high-energy laser systems, Opt. Mater. (Amsterdam, Neth.) 33(3) (2011) 511-518.

[17] E. Strassburger, Ballistic testing of transparent armour ceramics, J. Eur. Ceram. Soc. 29(2) (2009) 267-273.

[18] M. Suárez, A. Fernández, R. Torrecillas, J. Menéndez, Sintering to Transparency of Polycrystalline Ceramic Materials, in: A. Lakshmanan (Ed.), Sintering of Ceramics - New Emerging Techniques, InTech, Rijeka, Croatia, 2012, pp. 527-553.

[19] J.G.J. Peelen, R. Metselaar, Light scattering by pores in polycrystalline materials: Transmission properties of alumina, J. Appl. Phys. (Melville, NY, U.S.) 45(1) (1974) 216-220.

[20] S.F. Wang, J. Zhang, D.W. Luo, F. Gu, D.Y. Tang, Z.L. Dong, G.E.B. Tan, W.X. Que, T.S. Zhang, S. Li, L.B. Kong, Transparent ceramics: Processing, materials and applications, Prog. Solid State Chem. 41(1) (2013) 20-54.

[21] G. Zhang, D. Carloni, Y. Wu, Ultraviolet emission transparent Gd:YAG ceramics processed by solid-state reaction spark plasma sintering, Journal of the American Ceramic Society 103(2) (2020) 839-848.

[22] M. Stuer, Transparent Polycrystalline Alumina Processing, Sintering and Microstructural Analysis, EPFL, 2012.

[23] J.G.J. Peelen, Alumina : sintering and optical properties, Department of Chemical Engineering and Chemistry, Technische Hogeschool Eindhoven, Eindhoven, 1977, p. 99.

[24] A. Pille, M. Amamra, A. Kanaev, F. Schoenstein, Microstructure and optical properties of alumina sintered from various phases, Ceram. Int. 45(7, Part B) (2019) 9625-9630.

[25] X. Zhang, S. Liang, H. Li, J. Yang, Mechanical and optical properties of transparent alumina obtained by rapid vacuum sintering, Ceram. Int. 43(1, Part A) (2017) 420-426.

[26] G. Mata-Osoro, J.S. Moya, C. Pecharroman, Transparent alumina by vacuum sintering, Journal of the European Ceramic Society 32(11) (2012) 2925-2933.

[27] I.K. Jones, Z.M. Seeley, N.J. Cherepy, E.B. Duoss, S.A. Payne, Direct ink write fabrication of transparent ceramic gain media, Optical Materials 75 (2018) 19-25.

[28] L. Rueschhoff, W. Costakis, M. Michie, J. Youngblood, R. Trice, Additive Manufacturing of Dense Ceramic Parts via Direct Ink Writing of Aqueous Alumina Suspensions, International Journal of Applied Ceramic Technology 13(5) (2016) 821-830.

[29] S. Mamatha, P. Biswas, P. Ramavath, D. Das, R. Johnson, 3D printing of complex shaped alumina parts, Ceramics International 44(16) (2018) 19278-19281.

[30] M. Schwentenwein, J. Homa, Additive Manufacturing of Dense Alumina Ceramics, International Journal of Applied Ceramic Technology 12(1) (2015) 1-7.

[31] A. Krell, P. Blank, H. Ma, T. Hutzler, M.P.B. van Bruggen, R. Apetz, Transparent Sintered Corundum with High Hardness and Strength, J. Am. Ceram. Soc. 86(1) (2003) 12-18.

[32] S. Grasso, H. Yoshida, H. Porwal, Y. Sakka, M. Reece, Highly transparent α-alumina obtained by low cost high pressure SPS, Ceram. Int. 39(3) (2013) 3243-3248.

[33] J.A. Lewis, J.E. Smay, J. Stuecker, J. Cesarano, Direct Ink Writing of Three-Dimensional Ceramic Structures, Journal of the American Ceramic Society 89(12) (2006) 3599-3609.

[34] J. Cesarano, A Review of Robocasting Technology, MRS Proceedings 542 (1998) 133.

[35] I. Cesarano, Joseph, P.D. Calvert, Freeforming objects with low-binder slurry, in: U.S.P.a.T. Office (Ed.) United States Patent and Trademark Office, Sandia Corporation, United States, 2000.

[36] S.A. Wilson, L.M. Cross, C.W. Peak, A.K. Gaharwar, Shear-Thinning and Thermo-Reversible Nanoengineered Inks for 3D Bioprinting, ACS Appl. Mater. Interfaces 9(50) (2017) 43449-43458.

[37] R.A. Rezende, P.J. Bártolo, A. Mendes, R.M. Filho, Rheological behavior of alginate solutions for biomanufacturing, J. Appl. Polym. Sci. 113(6) (2009) 3866-3871.

[38] B.-N. Kim, A. Dash, Y.-W. Kim, K. Morita, H. Yoshida, J.-G. Li, Y. Sakka, Low-temperature spark plasma sintering of alumina by using SiC molding set, J. Ceram. Soc. Jpn. 124(10) (2016) 1141-1145.

[39] Q. Yang, Z. Zeng, J. Xu, H. Zhang, J. Ding, Effect of La2O3 on Microstructure and Transmittance of Transparent Alumina Ceramics, J. Rare Earths 24(1) (2006) 72-75.

[40] M. Fox, Optical Properties of Solids, Oxford University Press, New York, 2001.